Soft Matter

Polyelectrolyte Complex Films Influence the Formation of Polycrystalline Micro-Structures

Journal:	*Soft Matter*
Manuscript ID	SM-ART-12-2017-002466.R2
Article Type:	Paper
Date Submitted by the Author:	02-Apr-2018
Complete List of Authors:	Nakouzi, Elias; Florida State University, Department of Chemistry and Biochemistry Fares, Hadi; Florida State University College of Arts and Sciences, Chemistry & Biochemistry Schlenoff, Joseph; The Florida State University, Department of Chemistry and Biochemistry Steinbock, Oliver; Florida State University, Department of Chemistry and Biochemistry

Soft Matter

ARTICLE

Polyelectrolyte Complex Films Influence the Formation of Polycrystalline Micro-Structures

Received 00th January 20xx,
Accepted 00th January 20xx

DOI: 10.1039/x0xx00000x

www.rsc.org/

Elias Nakouzi†, Hadi M. Fares, Joseph B. Schlenoff, and Oliver Steinbock*

Silica-carbonate biomorphs are inorganic materials composed of thousands of crystalline nanorods that assemble complex morphologies such as helices, vessels, and sheets. We investigate the effect on biomorph crystallization of polyelectrolyte complex films that are prepared using the layer-by-layer deposition technique and post-processed to obtain three stable, chemically distinct films. Biomorph growth on poly(diallyldimethylammonium)-dominated substrates (cationic) shows polycrystalline helical and sheet structures bounded by large witherite prisms. Crystallization on poly(styrenesulfonate)-dominated (anionic) and stoichiometric substrates follows a qualitatively different pathway. We observe islands of radial mineral films that over several days extend at a remarkably constant velocity of 0.48 µm/h and eventually mineralize the whole substrate. Our work opens exciting avenues for the use of polyelectrolyte films as tunable substrates for biomimetic crystallization.

Introduction

Life has created sophisticated pathways for the assembly of nanocrystalline building blocks into complex, functional biominerals.[1] These structures pose an exciting challenge for modern materials science: can we develop bio-inspired pathways for building nanocrystals into hierarchically ordered structures and devices?[2] In this context, silica-carbonate biomorphs are an intriguing model system.[3-7] Biomorphs are purely inorganic precipitates of alkaline earth metal carbonates and amorphous silica. Despite their simple chemistry, biomorphs grow into complex micro-structures such as helices, sheets, funnels, and twisted wires that defy typical euhedral geometries. At the nanoscale, they consist of crystalline nanorods that assemble hierarchical architectures comparable to natural biominerals. Understanding and controlling this assembly process will lead to important advancements in bio-inspired materials synthesis.[7-11]

A crucial step is the ability to rationally design biomorphs with defined morphologies; a goal which to date has been met only partly. Biomorphs are typically grown in solution-gel or gas-diffusion setups wherein the diffusion of the reactant species across pH and concentration gradients produces a wealth of surprising precipitation patterns.[12, 13] Noorduin et al. showed that varying the flux of carbon dioxide into the reaction medium causes sharp transitions between different biomorph shapes.[13] Biomorph patterns are also strongly influenced by additives in the crystallization solution.[14-16] For example, solution polycationic species such as cetrimonium bromide (CTAB) surfactant and poly(diallyldimethylammonium) (PDADMA) induce the transition from classical biomorphs to spherulitic structures.[15] Similar effects were observed in the presence of acidic proteins known to regulate natural biomineralization.[17] These variations were broadly ascribed to the interaction of the additives with the negatively charged silicate species, but the mechanistic details have not been elucidated yet.

In this work we investigate the crystallization of biomorphs of silica and barium carbonate on polyelectrolyte complex films. These highly versatile thin films have been deployed in a variety of applications including tissue engineering, battery technology, and gas separation.[18] One particularly ambitious effort involved the assembly of a nacre-like material by the layered deposition of polymers and calcium carbonate.[19, 20] Other studies have focused on assembling polymeric multilayers on mineral surfaces or the sequential deposition of polymers and minerals to create inorganic-organic hybrid materials[21-27] that facilitate drug-delivery,[28] protein adsorption,[29] or bone regeneration.[30, 31] By comparison, the use of polyelectrolyte complex films as substrates for controlling crystallization has remained significantly unexplored,[32-36] partly because earlier methods for multilayer assembly produced films that are not completely stable in salt solutions.[37] In principle, the range of tunable physical and chemical parameters in these organic films should present ample possibilities for directing crystallization mechanisms and structures, thus granting a level of control comparable to the effectiveness of templating substrates in natural biomineralization.[1]

Address: Department of Chemistry and Biochemistry, Florida State University, Tallahassee, FL 32306-4390, USA
† Current address: Physical and Computational Sciences Directorate, Pacific Northwest National Laboratory, Richland, WA 99352, USA
Electronic Supplementary Information (ESI) available: experimental details on polymer film assembly, micrographs, and additional analyses. Two videos on mineral film disintegration. See DOI: 10.1039/x0xx00000x

Experimental

Assembly of polyelectrolyte complex films

We assemble polyelectrolyte multilayers using the layer-by-layer technique (Fig. 1),[37, 38] by dipping a glass slide or silicon wafer alternately into solutions of poly(diallyldimethylammonium) (PDADMA), a polycation with a quaternary ammonium group, and poly(styrenesulfonate) (PSS), a polyanion with a sulfonate group, with cycles of water rinsing in between (polyelectrolyte dipping: 5 min; water rinse: 3 × 1 min). In particular, we use both a 10 mM PDADMA (400,000–500,000 g/mol, Sigma-Aldrich) and 10 mM PSS (79,000 g/mol, Sigma-Aldrich) with respect to the monomer units, both prepared in 1 M NaCl (Fisher Scientific) solutions to build 20-, 30-, and 40-layers. These as-made multilayers are known to contain an excess of the polycation (PDADMA). Hence, we use a recently reported post-processing method to obtain three types of stable films: PDADMA-dominated films with an excess of approximately 35% ammonium groups, PSS-dominated films with 35% more sulfonate groups, and stoichiometric films in which the functional groups are mutually compensated as confirmed by infrared spectroscopy (Fig. 2).[38, 39] Depending on the number of layers added, the films have a wet thickness of 300–750 nm.

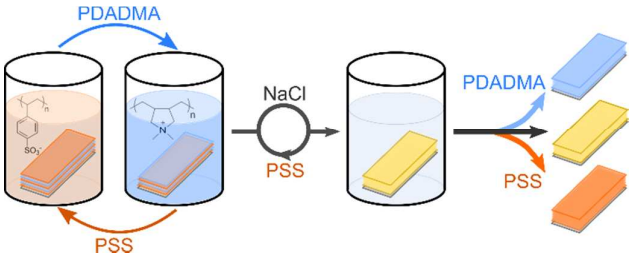

Fig. 1 Preparation and processing steps to produce three types of polyelectrolyte complex films. Color code is consistent throughout figures in manuscript and indicates PDADMA-dominated (blue), PSS-dominated (red), and stoichiometric (yellow) films.

Biomorph crystallization

In the next experimental step, we place the polyelectrolyte complex films in crystallization solutions of 5 mM barium chloride (Fisher Scientific) and 8.4 mM sodium metasilicate (Fisher Scientific). The pH is adjusted to 10.2–11 by adding a few drops of 0.1 M NaOH (Sigma-Aldrich). In one set of experiments, the reaction solutions are subjected to the influx of atmospheric carbon dioxide, which increases the supersaturation of barium carbonate and induces the co-precipitation of $BaCO_3$ and SiO_2. We also conduct experiments using the recently reported single-phase method, in which sodium carbonate (Mallinckrodt Chemicals) is added directly to the reaction medium (0.1–0.3 mM), and the pre-purged solutions are sealed from air to eliminate macroscale gradients in pH and carbonate concentration.[40]

Materials characterization

Optical microscopy images of the resulting biomorphs are obtained using a Nikon Elements Ti inverted microscope equipped with a Photometrics Coolsnap HQ2 camera. We collect electron micrographs using an FEI Nova 400 Field Emission Scanning Electron Microscope (FE-SEM) operating at 10–20 kV, after coating with a 4 nm layer of iridium using a Cressington HR 208 sputter coater. Molar percent chemical compositions are measured using an INCA energy dispersive X-ray spectroscopy (EDS) detector. Atomic force microscopy measurements of the growth thickness and surface roughness are performed on dry mineralized substrates in the amplitude modulated mode using an Asylum MFP3D microscope and an Olympus AC160TS-R3 probe. To obtain X-ray diffraction measurements (PXRD), we use a PANalytical X'pertPRO operated at the CuKα emission line with 0.0167° steps. Finally, infrared spectroscopy (IR) data are measured in the attenuated total reflectance mode using PerkinElmer Spectrum 100 FT-IR Spectrometer.

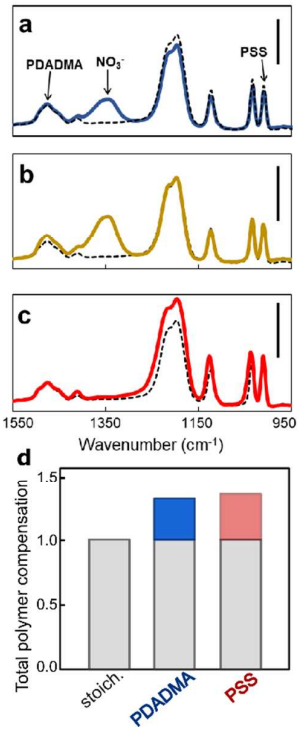

Fig. 2 Polymer films used as substrates. (a) 20-layer PDADMA/PSS film (solid blue line) and the same film after six cycles between 2 M NaCl for 30 min and 10 mM PSS in 1 M NaCl for 5 min (dashed line). (b) Cycled film (dashed line) and the same film after soaking in 10 mM PDADMA in 1 M NaCl for 3 h (solid yellow line). (c) Cycled film (dashed line) and the same film after soaking in 10 mM PSS and 1.4 M NaCl for 8 h (solid red line). Scale bars are 0.07 absorbance units. Nitrate layer indicates PDADMA excess (d) Bar graph representing the relative excess of PDADMA or PSS groups in each film as obtained from infrared spectroscopy.

Results and discussion

An important feature of our approach is that the polyelectrolyte complex films are relatively stable in solutions of low salt activity over extended periods of time, thus allowing for controlled crystallization experiments. Figure 3 shows the different morphologies obtained by biomorph crystallization on PDADMA-dominated films. The growth produces classical biomorph shapes, including sheets (Fig. 3a) and double helices (Fig. 3b,c). Garcia-Ruiz et al. demonstrated that all of these structures originate from barium carbonate single crystals that initially grow by the rod-fractal-dumbbell pathway.[5, 7] Subsequently, thousands of aligned nanorods emerge from the globules and form sheets whose edges curl into the bulk solution to nucleate single or double helices. In contrast to classical biomorphs, we observe within a few hours an overgrowth of larger microcrystals that show characteristic witherite crystal habits (Fig. 3a-c). The shape transition is accompanied by a sharp decrease in silica content from ~40% in the nanorod region to <5% in the larger prisms as measured by energy dispersive X-ray spectroscopy (EDS).

Similar results have been observed in some cases of polymer-free biomorph crystallization after ageing for several days. By comparison, the effect is much more pronounced, reproducible, and occurs within few hours of biomorph growth on PDADMA-dominated films. One possible explanation is that positively charged PDADMA interacts primarily with the negatively charged silica species. Accordingly, the rate of silica co-precipitation decreases and the barium carbonate crystals continue to grow to large-scale prisms. Note that silica colloids are negatively charged in high pH solutions as a result of the silanol surface groups,[41] while barium carbonate has an isoelectric point of pH ~10 and is hence expected to be neutral or only slightly negative.[42] In this context, Bauer et al. showed that high molecular weight polycations such as PDADMA readily adsorb on silica colloids at similar conditions and stabilize them against flocculation.[41] Similar interactions in our system can disrupt the growth of silica-carbonate biomorphs in favor of classical barium carbonate crystals. Our hypothesis is further supported by control experiments of barium carbonate crystallization on PDADMA surfaces in the absence of silicate (Fig. S1). We observe typical witherite morphologies with no clear influence of the polymer substrate on the growth rate or crystal habit.

Interestingly, the constituent nanorods of the biomorph sheets are not aligned along a single orientation (Fig. 3d). To characterize this feature, we perform a Fourier transform analysis on a sheet micrograph and obtain a power spectrum with a cross-shaped pattern (Fig. 3e). Figure 3f plots the intensity values from the power spectrum as a function of the azimuthal angle ϕ, where ϕ = 0 represents the approximate growth direction. The data are well-described by two Gaussian functions centered on -22.15° and 22.15°, suggesting the presence of two preferred alignment directions (Fig. 3f). Note that we do not conclusively ascribe this effect to the underlying polymer substrate, as similar patterns are occasionally observed in typical biomorph sheets.

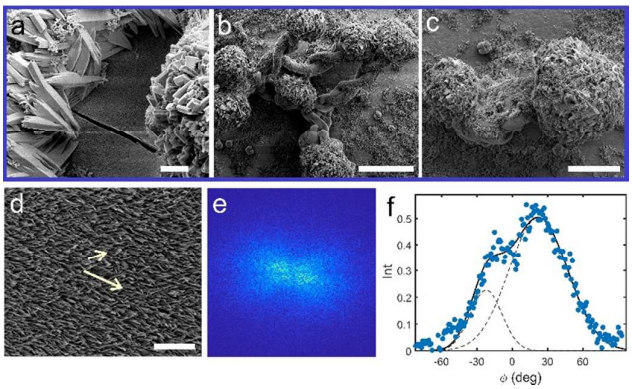

Fig. 3 (a-c) Scanning electron microscopy images of polycrystalline biomorphs and excessive witherite overgrowth on PDADMA-dominated film, (d) nanoscale texture of biomorph sheet. (e) Fourier transform of the nanorod pattern. (f) Plot of intensity values from the power spectrum as a function of the azimuthal angle ϕ. Data represented by double Gaussian function (continuous, black curve). Scale bars: (a, b) 50 µm, (c, d) 2 µm.

In contrast to the results described above, the crystallization on PDADMA/PSS stoichiometric substrates follows a qualitatively different pathway. Typical biomorphs are produced less frequently, and we mainly observe island structures with radially symmetric patterns (Fig. 4a-c). These islands consist of curved bundles, whose outer edges branch directly into the underlying substrate, suggesting strong polymer-reactant interactions that obstruct the formation of euhedral crystals or conventional nanorods (Fig. 4b, c, S2). The islands emerge from barium carbonate globules similar to classical biomorphs and expand at an initial velocity of ~0.097 µm/min. Similar morphologies are obtained by crystallization on the third type of substrates, namely the PSS-dominated multilayers (Fig. 4d-f). However, microscale features on the polymer surfaces cause fractures in the island patterns to create irregular morphologies. An example is shown in Fig. 4d,e where the barium carbonate globules are surrounded by island patterns that are not radially symmetric.

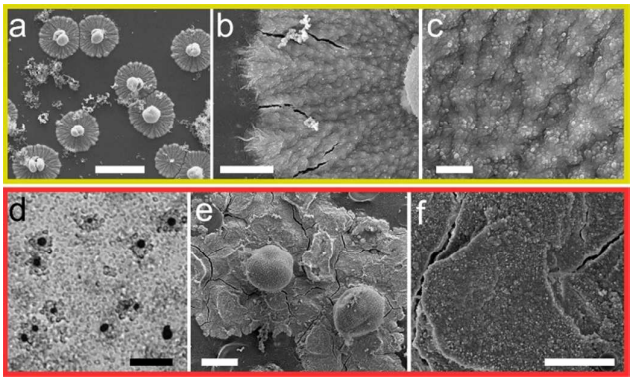

Fig. 4 (a-c) SEM images of biomorphs formed on the stoichiometric films. (d) Optical and (e, f) SEM images of biomorphs formed on PSS-dominated films. Scale bars: (a) 20 µm, (b, f) 2 µm, (c) 500 nm, (d) 50 µm, (e) 5 µm.

In the following discussion, we focus on characterizing the radial island structures that form on the stoichiometric polymer films. For this purpose, we performed crystallization experiments using the single-phase method that has been shown to facilitate biomorph growth up to millimeter length scales.[43] Using this method, the island structures continue to grow for several days and eventually expand to create a mineral film (Fig. 5a, b). These structures are in some ways comparable to calcium carbonate nanofilms that can form in the presence of soluble and templating polymers.[44-49] However, we emphasize that this effect is only observed here in the presence of both the polymer substrate and the silicate ions. In the absence of silicate, witherite microcrystals form on the polymer film and show typical euhedral shapes.

Figure 5c shows the expansion of four representative island structures (different color markers) with an average velocity of 0.48 µm/h (solid, black line). Remarkably, the growth velocity of the material remains constant for more than 120 hours. By comparison, biomorph sheets grown under similar solution conditions but without the underlying polymer expand with a velocity of 41 µm/h (dashed, red line); i.e. two orders of magnitude faster.[8, 50] We emphasize that the growth of these expansive mineral films is only possible in the single-phase system that allows continuous, stable crystallization over several days. In the gas-diffusion system, the mineral film growth slows down significantly and ceases within approximately two hours (inset, Fig. 5c). The continuous, black curve in Fig. 5c inset plots a square root fit to the data points at the early growth stages.

Measurements using atomic force microscopy (AFM) show that the mineral film has a thickness of (166 ± 39) nm and a local roughness of (27.9 ± 4.0) nm, measured over 2500 nm^2 film areas. Interestingly, when two growing regions approach, they do not overlap or contact. Instead, they simply cease growth abruptly, leaving a gap of approximately (276 ± 90) nm (Fig. 5b). This gap might be caused by an unidentified inhibitory species that is present along the entire growth front but reaches wave-terminating concentrations only in the collision zone where its diffusive influx occurs from two different directions. A similar phenomenon exists in certain bacterial colonies, for which it has been successfully simulated based on a simple reaction-diffusion model.[51] As a result, the mineral film covers the whole polymer substrate, but remains segmented into different domains. The pattern in Fig. 5e is reminiscent of segmented reaction-diffusion waves in the Belousov-Zhabotinsky reaction[52] but any mechanistic similarity must be strongly limited due to the absence of global oscillations and recovery dynamics in the biomorph system.

Table 1 summarizes the geometric features of the resulting structures. It is important to note that this growth behavior depends on the thickness of the polyelectrolyte substrate. Specifically, classical biomorph sheets form on 20- and 30-layer stoichiometric films, which have a thickness of 300 and 525 nm in millimolar salt solutions, respectively. However, the mineral film morphology is induced by 40-layer polymer substrates, which are 750 nm thick, or approximately 68 % the thickness of a biomorph sheet.

In contrast to typical biomorphs, the mineral film nanotexture consists of curved bundles instead of linear, rigid nanorods (Fig. 5). Moreover, the bundles create oscillatory features that appear as nearly concentric rings with an average spacing of (475 ± 28) nm (Fig. 5f); one order of magnitude smaller than the periodic height variations recently reported for biomorph sheets.[50] The presence of double peaks in corresponding power intensity plots indicates that the bundles are partially misaligned (arrows, Fig. 5f). The morphology is reminiscent of the so-called "sheaf-of-wheat" patterns reported for calcite crystals grown in silica gel at elevated pH levels.[53] In contrast to regular biomorph sheets, these structures do not show continuous cross-shaped birefringence patterns when viewed between two crossed polarizers (Fig. S3). The latter effect is ascribed to the markedly different nanoscale texture. Another important distinction from typical biomorphs is that the mineral films produced here remain strongly adhered to the polymer substrate, further indicating the role of polymer-reactant interactions in the growth process. Note that in the absence of the polymer substrate, biomorph sheets grown in the single-phase system typically curl upwards into the bulk solution to form funnels, vessels, or wavy curtain patterns.

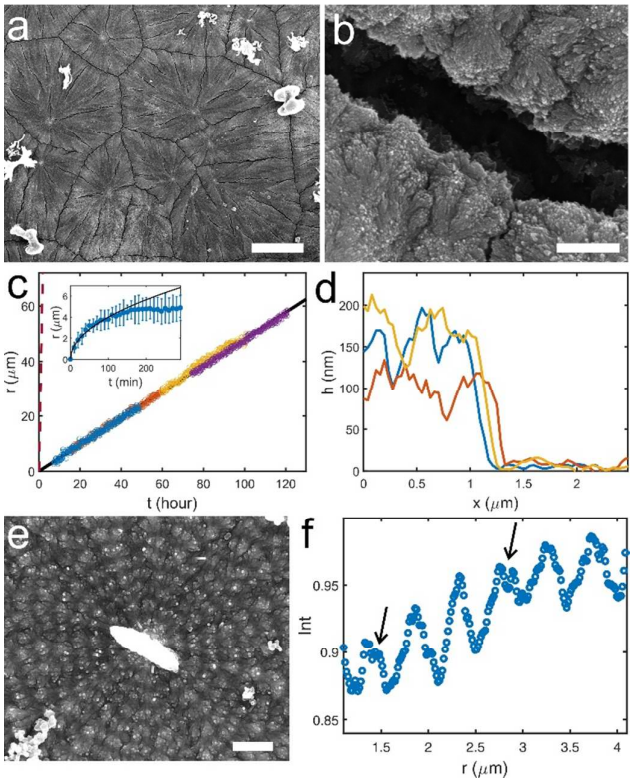

Fig. 5 (a-b) Micrographs of mineral films grown using the single-phase method. (c) Plot of film growth velocity in the single-phase system. Color markers denote different samples. Dashed, red line on the left side represents the average growth velocity of typical biomorph sheets. Inset shows growth of radial film in the gas diffusion system, with continuous, black curve representing a square root fit using data points until t = 100 min. (d) Height profiles of biomorph films. (e) Nanoscale texture of biomorph films. (f) Plot of intensity values from SEM image in (e) as a function of

distance from the globule in the center. Scale bars: (a) 10 µm, (b) 400 nm, (e) 1 µm.

An important question concerns the chemical nature of the mineral films. Analysis using attenuated total reflectance infrared (ATR-IR) spectroscopy confirms the presence of barium carbonate as indicated by the peaks at 1751, 1420, 857, and 690 cm^{-1} (Fig. 6a). We also observe the characteristic PSS (1185, 1130, 1042 cm^{-1}) and PDADMA (1470 cm^{-1}) peaks. In addition, X-ray diffraction measurements show the witherite reflections at 23.9°, 27.7°, 34.1°, 42.1°, 44.9°, and 46.8° (Fig. 6b). Elemental analysis (EDS) suggests relative molar percentages of (40.7 ± 5.6)% barium, (21.0 ± 8.6)% silicon, and (38.3 ± 13.9)% sulfur. The latter values may overestimate the sulfur due to a contribution from the underlying polymer. However, the measurements present lower bounds for the silicon and barium content, and provide evidence that the Ba:Si ratio is comparable to typical biomorphs, with the possible inclusion of polymeric species.

Our observations are further supported by a series of dissolution/disintegration experiments. Firstly, we subject a mineral film to mildly acidic conditions by adding a few drops of 0.1 M HCl on top of the grown structures. The film dissolves within seconds (Fig. 6c, supplementary video), thus validating the presence of barium carbonate. Notice that biomorph helices also dissolve leaving behind hollow shells of amorphous silica (arrow, Fig. 6c). In another experiment, we sinter a mineral film in a furnace at 500°C for five hours, which causes the polymeric material to disintegrate. Figure 6d shows that the circular patterns survive the heating process, providing further evidence of the inorganic nature of the material (Fig. 6d). Thirdly, we expose the mineral films to a solution of 2.5 M KBr. The high salt activity causes the dissociation of the polymeric films as the ions diffuse into the films and break the polymer-polymer interactions. Almost instantly, the circular patterns shrink and show radial cracks, as the polymer is released from the mineral film (arrow in Fig. 6e, supplementary video). This observation suggests that the polymeric material is incorporated within the mineral films and not simply a passive substrate.

Table 1. Geometric properties of mineral films

Film Property	Measured value
Thickness of polymer film in salt solution	~750 nm
Local roughness of mineral film	(27.9 ± 4.0) nm
Wavelength of oscillatory features	(475 ± 28) nm
Increase in thickness after mineralization	(166 ± 39) nm
Gap between adjacent film domains	(276 ± 90) nm
Film growth velocity	0.48 µm/h

Conclusions

Our study opens wider possibilities for the use of polyelectrolyte complex films as well-defined substrates that control biomimetic crystallization. In addition to subtle changes in the biomorph patterns on PDADMA-dominated substrates, we observe a qualitatively different behavior on stoichiometric and PSS-dominated substrates. The growing structures act as propagating fronts that leave in their wake a mineral film and eventually cover the whole surface. Moreover, the occurrence of these structures is determined by the thickness of the polymer film and the final pattern is influenced by microscale features on the polymer surface. We note that the resulting patterns differ markedly from classical biomorphs in terms of nanoscale texture, growth velocity, and characteristic features such as height oscillations. Instead of protruding into the bulk solutions, the mineral films remain bound strongly to the substrate, indicating the prominence of polymer-reactant interactions in the growth mechanism. Future studies should focus on understanding the specific interactions that are responsible for altering the crystallization mechanism. These systems should be studied in light of related pathways known as polymer induced liquid precursor (PILP) crystallization, which have produced fascinating structural and micro-engineering complexity – including metal carbonate films in the presence of soluble polymers[48, 54, 55]–but whose underlying mechanisms remain highly contentious.

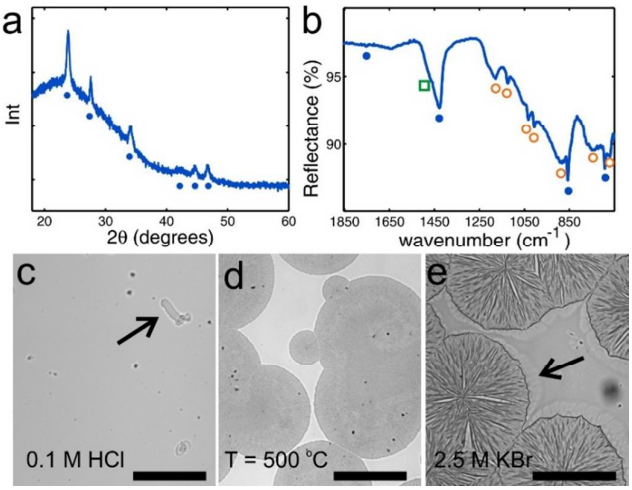

Fig. 6 (a) XRD and (b) IR spectra show barium carbonate (filled, blue circles), silica (green square), as well as the distinctive polymer peaks (open, orange circles). Images of film exposed to (c) acid, (d) high temperature, and (e) salt solution. Arrows highlight hollow silica shell in (c) and release of polymer material in (e). Scale bar: (c-e) 100 µm.

Finally, it is interesting to compare the polyelectrolyte complex films described here to self-assembled monolayers which have been studied extensively as substrates for crystallization.[13, 56, 57] Self-assembled monolayers offer a powerful degree of

control over nucleation density, crystal orientation, polymorph selection, and even the location of the growing crystals. This molecular-level precision is clearly not matched by polyelectrolyte complex films. However, the system reported here provides a range of useful control parameters including film thickness and local roughness, the synergistic activity of more than one functional group, confinement effects within the film, as well as the synthesis of inorganic-organic hybrid materials.[46, 58] We anticipate that the further exploration of these parameters will produce a plethora of biomimetic structures and emergent dynamic phenomena.

Conflicts of interest

There are no conflicts to declare.

Acknowledgements

This material is based upon work supported by the National Science Foundation under Grant No. DMR1609495 to OS and DMR1506824 to JBS. A portion of the data analysis was conducted under the Laboratory Directed Research and Development Program at Pacific Northwest National Laboratory, a multiprogram national laboratory operated by Battelle for the U.S. Department of Energy. EN is grateful for the support of the Linus Pauling Distinguished Postdoctoral Fellowship program. The Biological Science Imaging Resource (BSIR) User Facility at Florida State University provided access to the SEM instrument. We thank Dr. Susan Latturner and Dr. Ryan Groom for access to and assistance with the furnace instrument.

References

1. S. Mann, *Biomineralization: Principles and Concepts in Bioinorganic Materials Chemistry*, Oxford University Press, Oxford, UK, 2001.
2. E. Nakouzi and O. Steinbock, *Sci. Adv.*, 2016, **2**, e1601144, 1-13.
3. J. M. Garcia-Ruiz, S. T. Hyde, A. M. Carnerup, A. G. Christy, M. J. Van Kranendonk and N. J. Welham, *Science*, 2003, **302**, 1194-1197.
4. S. T. Hyde, A. M. Carnerup, A.-K. Larsson, A. G. Christy and J. M. García-Ruiz, *Phys. A (Amsterdam, Neth.)*, 2004, **339**, 24-33.
5. J. M. Garcia-Ruiz, E. Melero-Garcia and S. T. Hyde, *Science*, 2009, **323**, 362-365.
6. G. Zhang, J. Morales and J. M. García-Ruiz, *J. Mater. Chem. B*, 2017, **5**, 1658-1663.
7. M. Kellermeier, H. Cölfen and J. M. García-Ruiz, *Eur. J. Inorg. Chem.*, 2012, **2012**, 5123-5144.
8. M. Kellermeier, E. Melero-Garcia, F. Glaab, J. Eiblmeier, L. Kienle, R. Rachel, W. Kunz and J. M. Garcia-Ruiz, *Chemistry*, 2012, **18**, 2272-2282.
9. C. N. Kaplan, W. L. Noorduin, L. Li, R. Sadza, L. Folkertsma, J. Aizenberg and L. Mahadevan, *Science*, 2017, **355**, 1395-1399.
10. M. Montalti, G. Zhang, D. Genovese, J. Morales, M. Kellermeier and J. M. Garcia-Ruiz, *Nat. Commun.*, 2017, **8**, 14427, 1-6.
11. J. Opel, F. P. Wimmer, M. Kellermeier and H. Cölfen, *Nanoscale Horiz.*, 2016, **1**, 144-149.
12. E. Melero-García, R. Santisteban-Bailón and J. M. García-Ruiz, *Cryst. Growth Des.*, 2009, **9**, 4730-4734.
13. W. L. Noorduin, A. Grinthal, L. Mahadevan and J. Aizenberg, *Science*, 2013, **340**, 832-837.
14. E. Nakouzi, R. Rendina, G. Palui and O. Steinbock, *J. Cryst. Growth*, 2016, **452**, 166-171.
15. M. Kellermeier, F. Glaab, A. M. Carnerup, M. Drechsler, B. Gossler, S. T. Hyde and W. Kunz, *J. Cryst. Growth*, 2009, **311**, 2530-2541.
16. A. E. Voinescu, M. Kellermeier, B. Bartel, A. M. Carnerup, A. Larsson, D. Touraud, W. Kunz, L. Kienle, A. Pfitzner and S. T. Hyde, *Cryst. Growth Des.*, 2008, **8**, 1515-1521.
17. N. Sánchez-Puig, E. Guerra-Flores, F. López-Sánchez, P. A. Juárez-Espinoza, R. Ruiz-Arellano, R. González-Muñoz, R. Arreguín-Espinosa and A. Moreno, *J. Mater. Sci.*, 2011, **47**, 2943-2950.
18. J. J. Richardson, M. Bjornmalm and F. Caruso, *Science*, 2015, **348**, aaa2491.
19. Z. Tang, N. A. Kotov, S. Magonov and B. Ozturk, *Nat. Mater.*, 2003, **2**, 413-418.
20. M. Rubner, *Nature*, 2003, **423**, 925-926.
21. J. Li, Z. Y. Jiang, H. Wu, L. Zhang, L. H. Long and Y. J. Jiang, *Soft Matter*, 2010, **6**, 542-550.
22. Y. J. Jiang, D. Yang, L. Zhang, Q. Y. Sun, X. H. Sun, J. Li and Z. Y. Jiang, *Adv. Funct. Mater.*, 2009, **19**, 150-156.
23. I. F. Patel, M. V. Kiryukhin, N. L. Yakovlev, H. S. Gupta and G. B. Sukhorukov, *J. Mater. Chem. B*, 2015, **3**, 4821-4830.
24. G. H. Liu, Z. Y. Jiang, X. X. Cheng, C. Chen, H. Yang, H. Wu, F. S. Pan, P. Zhang and X. Z. Cao, *J. Membr. Sci.*, 2016, **520**, 364-373.
25. Y. L. Lee, T. X. Lin, F. M. Hsu and J. S. Jan, *Nanoscale*, 2016, **8**, 2367-2377.
26. T. Serizawa, T. Tateishi, D. Ogomi and M. Akashi, *J. Cryst. Growth*, 2006, **292**, 67-73.
27. Á. J. Leite, P. Sher and J. F. Mano, *Mater. Lett.*, 2014, **121**, 62-65.
28. J. Wei, J. Shi, Q. Wu, L. Yang and S. K. Cao, *J. Mater. Chem. B*, 2015, **3**, 8162-8169.
29. W. L. Gao, B. Feng, Y. X. Ni, Y. L. Yang, X. O. Lu and J. Weng, *Appl. Surf. Sci.*, 2010, **257**, 538-546.
30. S. R. Pattabhi, A. M. Lehaf, J. B. Schlenoff and T. C. S. Keller, *J. Biomed. Mater. Res., Part A*, 2015, **103**, 1818-1827.
31. H. Rammal, M. Dubus, L. Aubert, F. Reffuveille, D. Laurent-Maquin, C. Terryn, P. Schaaf, H. Alem, G. Francius, F. Quiles, S. C. Gangloff, F. Boulmedais and H. Kerdjoudj, *ACS Appl. Mater. Interfaces*, 2017, **9**, 12791-12801.
32. C. H. Lu, L. M. Qi, J. M. Ma, H. M. Cheng, M. F. Zhang and W. X. Cao, *Langmuir*, 2004, **20**, 7378-7380.
33. A. K. Dutta, G. Jarero, L. Q. Zhang and P. Stroeve, *Chem. Mater.*, 2000, **12**, 176-181.

34. K. Abdelkebir, S. Morin-Grognet, F. Gaudiere, G. Coquerel, B. Labat, H. Atmani and G. Ladam, *Acta Biomater.*, 2012, **8**, 3419-3428.
35. P. A. Ngankam, P. Lavalle, J. C. Voegel, L. Szyk, G. Decher, P. Schaaf and F. J. G. Cuisinier, *J. Amer. Chem. Soc.*, 2000, **122**, 8998-9005.
36. V. Ball, M. Michel, F. Boulmedais, J. Hemmerle, Y. Haikel, P. Schaaf and J. C. Voegel, *Cryst. Growth Des.*, 2006, **6**, 327-334.
37. H. M. Fares, Y. E. Ghoussoub, R. L. Surmaitis and J. B. Schlenoff, *Langmuir*, 2015, **31**, 5787-5795.
38. H. M. Fares and J. B. Schlenoff, *Macromolecules*, 2017, **50**, 3968-3978.
39. H. M. Fares and J. B. Schlenoff, *J. Am. Chem. Soc.*, 2017, **139**, 14656-14667.
40. E. Nakouzi, P. Knoll and O. Steinbock, *Chem. Commun. (Camb)*, 2016, **52**, 2107-2110.
41. D. Bauer, E. Killman and W. Jaeger, *Colloid. Polym. Sci.*, 1998, **276**, 698-708.
42. C. C. Li and J. J. Jean, *J. Am. Ceram. Soc.*, 2002, **85**, 2977–2983.
43. E. Nakouzi, P. Knoll, K. B. Hendrix and O. Steinbock, *Phys. Chem. Chem. Phys.*, 2016, **18**, 23044-23052.
44. T. Kato, *Adv. Mater.*, 2000, **12**, 1543-1546.
45. E. DiMasi, M. J. Olszta, V. M. Patel and L. B. Gower, *CrystEngComm*, 2003, **5**, 346-350.
46. C. Xiao, M. Li, B. Wang, M. F. Liu, C. Shao, H. Pan, Y. Lu, B. B. Xu, S. Li, D. Zhan, Y. Jiang, R. Tang, X. Y. Liu and H. Cölfen, *Nat. Commun.*, 2017, **8**, 1398, 1-9.
47. E. DiMasi, S. Y. Kwak, F. F. Amos, M. J. Olszta, D. Lush and L. B. Gower, *Phys. Rev. Lett.*, 2006, **97**, 045503.
48. L. B. Gower and D. K. Odom, *J. Cryst. Growth*, 2000, **210**, 719-734.
49. D. Volkmer, M. Harms, L. B. Gower and A. Ziegler, *Angew. Chem. Int. Ed. Engl.*, 2005, **44**, 639-644.
50. E. Nakouzi, Y. E. Ghoussoub, P. Knoll and O. Steinbock, *J. Phys. Chem. C*, 2015, **119**, 15749-15754.
51. A. Be'er, H. P. Zhang, E.-L. Florin, S. M. Payne, E. Ben-Jacob and H. L. Swinney, *Proc. Natl. Acad. Sci. USA*, 2009, **106**, 428-433.
52. V. K. Vanag and I. R. Epstein, *Proc. Natl. Acad. Sci. USA*, 2003, **100**, 14635-14638.
53. S. Dominguez Bella and J. M. Garcia-Ruiz, *J. Mater. Sci.*, 1987, **22**, 3095-3102.
54. L. B. Gower and D. A. Tirrell, *J. Cryst. Growth*, 1998, **191**, 153-160.
55. S. J. Homeijer, R. A. Barrett and L. B. Gower, *Crystal Growth & Design*, 2010, **10**, 1040-1052.
56. J. Aizenberg, A. J. Black and G. M. Whitesides, *Nature*, 1999, **398**, 495-498.
57. J. C. Love, L. A. Estroff, J. K. Kriebel, R. G. Nuzzo and G. M. Whitesides, *Chem. Rev.*, 2005, **105**, 1103-1169.
58. H. Li, H. L. Xin, D. A. Muller and L. A. Estroff, *Science*, 2009, **326**, 1244-1247.

Biomorphs are life-like, inorganic microshapes of hierarchically ordered nanoparticles and their growth can be controlled by the use of tunable polyelectrolyte films.

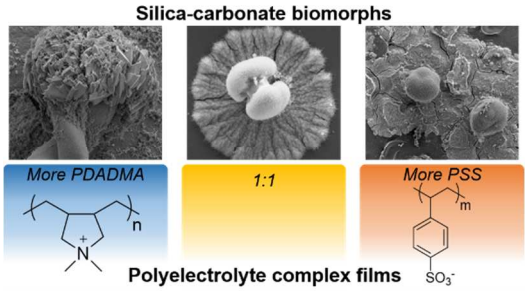

TOC graphic